AFRL-PR-WP-TP-2006-230

PARTIAL MELT PROCESSING OF SOLID-SOLUTION $Bi_2Sr_2CaCu_2O_{8+\delta}$ THICK-FILM CONDUCTORS WITH NANOPHASE Al_2O_3 ADDITIONS (POSTPRINT)

T. Haugan, W. Wong-Ng, L.P. Cook, M.D. Vaudin,
L. Swartzendruber, and P.N. Barnes

APRIL 2006

Approved for public release; distribution is unlimited.

STINFO COPY

PROPULSION DIRECTORATE
AIR FORCE MATERIEL COMMAND
AIR FORCE RESEARCH LABORATORY
WRIGHT-PATTERSON AIR FORCE BASE, OH 45433-7251

REPORT DOCUMENTATION PAGE

Form Approved
OMB No. 0704-0188

1. REPORT DATE *(DD-MM-YY)*	2. REPORT TYPE	3. DATES COVERED *(From - To)*
April 2006	Journal Article Postprint	04/01/2002 – 04/01/2002

4. TITLE AND SUBTITLE

PARTIAL MELT PROCESSING OF SOLID-SOLUTION $Bi_2Sr_2CaCu_2O_{8+\delta}$ THICK-FILM CONDUCTORS WITH NANOPHASE Al_2O_3 ADDITIONS (POSTPRINT)

5a. CONTRACT NUMBER
In-house

5b. GRANT NUMBER

5c. PROGRAM ELEMENT NUMBER
61102F/62203F

6. AUTHOR(S)

T. Haugan and P.N. Barnes (AFRL/PRPG)
W. Wong-Ng, L.P. Cook, M.D. Vaudin, and L. Swartzendruber (National Institute of Standards and Technology)

5d. PROJECT NUMBER
3145

5e. TASK NUMBER
32

5f. WORK UNIT NUMBER
31453279

7. PERFORMING ORGANIZATION NAME(S) AND ADDRESS(ES)

Power Generation Branch (AFRL/PRPG)
Power Division
Propulsion Directorate
Air Force Research Laboratory, Air Force Materiel Command
Wright-Patterson Air Force Base, OH 45433-7251

National Institute of Standards and Technology
Materials Science and Engineering Laboratory
100 Bureau Dr. Stop 8520
Gaithersburg, MD 20899-8520

8. PERFORMING ORGANIZATION REPORT NUMBER
AFRL-PR-WP-TP-2006-230

9. SPONSORING/MONITORING AGENCY NAME(S) AND ADDRESS(ES)

Propulsion Directorate
Air Force Research Laboratory
Air Force Materiel Command
Wright-Patterson AFB, OH 45433-7251

10. SPONSORING/MONITORING AGENCY ACRONYM(S)
AFRL-PR-WP

11. SPONSORING/MONITORING AGENCY REPORT NUMBER(S)
AFRL-PR-WP-TP-2006-230

12. DISTRIBUTION/AVAILABILITY STATEMENT
Approved for public release; distribution is unlimited.

13. SUPPLEMENTARY NOTES
Journal article postprint published in J. Mater. Res, Vol. 18, No. 5, May 2003, Materials Research Society, publisher.

PAO case number: ASC 02-3038; Date cleared: 27 Dec 2002.

14. ABSTRACT

Partial-melt processing of BiSrCaCuO thick-film conductors with additions of nanophase Al_2O_3 was studied to increase flux pinning and inhibit SrCaCuO phase defect formation. Nanophase Al_2O_3 was added to Bi:Sr:Ca:Cu:O powders with four different compositions: three with Bi:Cu approximately 2:2 and one closer to the ideal Bi-2223 composition. The effect of Al_2O_3 addition on film microstructural and superconducting properties was studied for a range of partial-melt temperatures. Results were compared to Al_2O_3-free films with compositions lying within the single-phase solid-solution 2212 region. Nanophase Al_2O_3 reacted with 2212-type precursors to form a composite of micron size or smaller particles of solid-solution $(Sr,Ca)_3Al_2O_6$ in a solid-solution 2212 superconducting matrix. The Ca content of the $(Sr,Ca)_3Al_2O_6$ in a solid-solution 2212 superconducting matrix. The Ca content of the $(Sr,Ca)_3Al_2O_6$ particles formed was approximately like 2212 precursor. Addition of 6-25% volume fraction of $(Sr,Ca)_3Al_2O_6$ to Bi-2212 only slightly reduced Tcs and c-axis texturing, but improved film quality by reducing Sr-Ca-Cu-O defect volume fraction by factors of 2 to 6 and significantly increased Jc by over one order of magnitude for 0 to 2 T applied fields at 20 to 30 K.

15. SUBJECT TERMS
Partial melt process, conductors, YBCO

16. SECURITY CLASSIFICATION OF:			17. LIMITATION OF ABSTRACT:	18. NUMBER OF PAGES	19a. NAME OF RESPONSIBLE PERSON (Monitor)
a. REPORT	b. ABSTRACT	c. THIS PAGE			Paul N. Barnes
Unclassified	Unclassified	Unclassified	SAR	20	19b. TELEPHONE NUMBER *(Include Area Code)* N/A

Standard Form 298 (Rev. 8-98)
Prescribed by ANSI Std. Z39-18

Partial melt processing of solid-solution $Bi_2Sr_2CaCu_2O_{8+\delta}$ thick-film conductors with nanophase Al_2O_3 additions

T. Haugan,[a] W. Wong-Ng, L.P. Cook, M.D. Vaudin, and L. Swartzendruber
National Institute of Standards and Technology, Materials Science and Engineering Laboratory, 100 Bureau Dr. Stop 8520, Gaithersburg, Maryland 20899-8520

P.N. Barnes
Air Force Research Laboratory, Propulsion Directorate, 2645 Fifth St., Ste. 13, Wright-Patterson AFB, Ohio 45433-7919

(Received 5 April 2002; accepted 14 January 2003)

Partial-melt processing of $Bi_{2+x}Sr_{2-x-y}Ca_{1+y}Cu_2O_{8+\delta}$ (Bi-2212) thick-film conductors with additions of nanophase Al_2O_3 was studied for dual purposes of increasing flux pinning and inhibiting Sr–Ca–Cu–O phase defect formation. Nanophase Al_2O_3 (<50% mole fraction) was added to Bi:Sr:Ca:Cu:O powders with four different compositions: three with Bi:Cu approximately 2:2 and one ($Bi_2Sr_{2.38}Ca_{1.15}Cu_{2.92}O_{9.7+\delta}$) closer to the ideal Bi-2223 composition. The effect of Al_2O_3 addition on film microstructural and superconducting properties was studied for a range of partial-melt temperatures (865 to 900 °C). Results were compared to Al_2O_3-free films with compositions lying within the single-phase solid-solution 2212 region. Nanophase Al_2O_3 reacted with 2212-type precursors to form a composite of micron size or smaller particles of solid-solution $(Sr,Ca)_3Al_2O_6$ in a solid-solution 2212 superconducting matrix. The Ca content of the $(Sr,Ca)_3Al_2O_6$ particles formed approximated that of the 2212 precursor ($\leqslant$6% mole fraction difference). Addition of 6–25% volume fraction of $(Sr,Ca)_3Al_2O_6$ to Bi-2212 (by reaction between Al_2O_3 and Bi-2212) only slightly reduced superconducting transition temperatures and *c*-axis texturing; however this addition improved film quality by reducing Sr–Ca–Cu–O defect volume fraction by factors of 2 to 6 and significantly increased the critical current density by over one order of magnitude for 0 to 2 T applied fields at 20 to 30 K.

I. INTRODUCTION

Thick-film or wire conductors of solid-solution $Bi_{2+x}Sr_{2-x-y}Ca_{1+y}Cu_2O_{8+\delta}$ (Bi-2212) superconductors are candidates for long-length power applications, because of their capability to be fabricated by lower cost methods such as thick-film coating on Ag or relatively inexpensive Ni and because of their high transport critical current density (J_c) > 10^5 A/cm^2 at $\leqslant$ 20 K in at least 0 to 3 T magnetic fields.[1–3] The Bi-2212 conductors are typically processed by a partial-melt method, where the precursor powder is brought above the melting temperature and then slowly cooled below the melting point.[4–6] An optimum time is generally required for melting, and the formation of large (approximately 20 to 200 μm length) second-phase defects during the nonequilibrium melting process has been noted by many authors.[6–8] These defects can reduce J_c by impeding the critical current flow.[9]

Because of intrinsically poor flux pinning, the operation temperature for Bi-2212 conductors is below 30 or 50 K for magnetic fields applied parallel or perpendicular, respectively, to the *c* axis of the Bi-2212 phase.[2,10] The limit for practical applications is generally referred to in temperature versus magnetic field space by the "irreversibility" or "melting" line, above which the superconductor does not support loss transport current due to flux motion.[2] However, with the addition of pinning defects by heavy ion (Sn) or 0.8-GeV proton irradiation, the irreversibility line of Bi-2212 was shifted approximately 20 K higher for applied magnetic fields >1 T in tapes or crystals, and the magnetic J_c at all temperatures and magnetic fields was improved.[2,11]

To increase flux-pinning in Bi-2212, the goal for this study was to use chemically simple processing methods to achieve a nonsuperconducting second-phase defect density on the order of approximately $(M/2) \times 10^{11}$ cm^{-2} to pin an applied magnetic field of strength *M* in Tesla.[2] This defect density would provide a pinning site for every flux quanta with strength $\phi_o = 2.07 \times 10^{-11}$ T cm^2. In a linear direction, the goal for defect density would be approximately $(M/2)^{0.5} \times 10^{5.5}$ cm^{-1}, or approximately *M*

[a]Address all correspondence to this author.
e-mail: timothy.haugan@wpafb.af.mil

defects in a spacing of 100 nm for *M* in the range of 3 to 7 T. With this criterion, pinning defects should be on the order of approximately 10 nm or less, with a smaller size preferred to allow a higher volume fraction of superconductor. While micron-sized defects have been shown to improve flux-pinning by creation of secondary defects such as dislocation networks with high density,[2] other studies show only nanometer (and not micron-) size defects are responsible for improvements in flux-pinning.[12]

In this paper, nanophase Al_2O_3 particles were considered for defect addition (in part) because they are commercially available in kilogram-size batches with low cost of approximately $135/kg (Nanophase Technologies Corp., Burr Ridge, IL). The materials cost of Al_2O_3 is lower than alternative materials that are typically considered for Bi–Sr–Ca–Cu–O applications and are available in nano-size, including Y_2O_3 (approximately $260/kg), ZrO_2 (approximately $1500/kg), MgO (approximately $6500/kg), or Ag (approximately $11,000/kg) (Nanophase Technologies Corp., Burr Ridge, IL; Alfa-Aesar, Ward Hill, MA). Any reduction in raw materials costs would be beneficial when considering production of km-length conductors.

The chemical reaction of Al_2O_3 with Bi-2212-type compounds has been observed in thick-film tapes processed on Ag foils,[13–15] in bulk compounds,[16–21] in fiber or single-crystal growth,[22–25] and in thick-film growth on Al_2O_3 substrates.[26] The reaction products observed in these studies were approximately identified as (listed in order of decreasing Al mole fraction % with Al content normalized to 2): ~$(Sr,Ca)_2Al_2O_x$;[22] ~$Bi_{0.4}(Sr,Ca)_{1.6}Al_2O_x$;[18] $(Sr,Ca)_3Al_2O_6$;[13–21,26] ~$Bi(Sr,Ca)_2Al_2O_6$;[16,19,24] ~$(Sr,Ca)_4Al_2O_x$;[15,18] ~$Bi_{1.33}(Sr,Ca)_{2.67}Al_2O_x$;[15] ~$Bi_2(Sr,Ca)_3(Cu,Al)_2O_x$.[24,26] Among these phases, solid-solution $(Sr,Ca)_3Al_2O_6$ and $Bi(Sr,Ca)_2Al_2O_6$ were shown to be chemically compatible with solid-solution Bi-2212 in $BiO_{1.5}$–SrO–CaO–CuO–$AlO_{1.5}$ subsolidus equilibrium phase space, for a limited range of compositions studied.[16,17,19] The combinations of equilibrium phases that potentially could form from reaction of Al_2O_3 and Bi–Sr–Ca–Cu–O are unknown, as phase equilibrium diagrams in multidimensional $BiO_{1.5}$–SrO–CaO–CuO–$AlO_{1.5}$ phase space are not yet available.[16]

The reaction products mentioned above show trends in chemical substitution and composition expected for intersubstitution of similar ionic radius[27] (e.g., Bi, Sr, and Ca for each other in solid solution and Al for Cu or vice-versa). Compositions of the Al-containing phases have only been measured approximately thus far, as reference x-ray diffraction (XRD) patterns of solid-solution compounds are not available in the powder diffraction file[28] and energy dispersive spectroscopic (EDS) measurements can be affected by complications such as x-ray fluorescence and mass absorption during analysis of submicron particles.[29]

In initial reports by our group and others, addition of nanophase Al_2O_3 was shown to improve 2212 film properties by inhibiting Sr–Ca–Cu–O defect formation[13–15] and increasing flux pinning.[13,14,18,19] With addition of nano-size Al_2O_3, there was minor or neglible degradation of 2212 superconducting properties, with variations depending on the specific processing conditions used.[13–15,18,19] In this paper, both of these effects are studied in more detail for a variety of solid-solution Bi-2212 compositions, with additional analysis provided of the chemical reaction of nanophase Al_2O_3 with Bi–Sr–Ca–Cu–O for different nonequilibrium melting conditions.

Solid phases identified in this work are shown in Table I. All of the phases exist as solid solutions, where Ca can substitute for Sr in the crystal structures.

II. EXPERIMENTAL

Precursor powders were prepared by the solid-state method, using starting reactants of Bi_2O_3, $SrCO_3$, $CaCO_3$, and CuO, all of purity >99.95%. Powders were mixed and ground with an agate mortar and pestle, calcined by heating from 650 to 830 °C at 25 °C/h, and subsequently annealed about 3–4 times at 830 to 860 °C in air, with intermediate grinding between annealings. Repeat annealings were performed until equilibrium was reached at the final annealing temperature of 860 °C, as determined by XRD. The powders were reacted in approximately 1-cm diameter pellets with 0.5 to 1.0 g batches, formed by lightly pressing in dies (approximately 10^7 Pa). Pellets were reacted on a bed of sacrificial powder on polycrystalline MgO supports. The slow-heating calcination step was used to eliminate intermediate melting reactions of sacrificial powder with MgO substrates and reduce formation of intermediate compounds.[6]

Powders of varying Bi:Sr:Ca:Cu:O composition were prepared for reaction with Al_2O_3 addition, as shown in Table II. Nanophase (γ,α)–Al_2O_3 powder (10 to 20 nm), 99.98% purity and density $\simeq$ 3.965 g/cm^3, purchased commercially (Alfa-Aesar, Ward Hill, MA) was added to four of the Bi-2212 powders in Table II (denoted with a

TABLE I. Chemical phases and corresponding symbols in this study.

Chemical formula	Symbol
$Bi_{2+x}Sr_{2-x-y}Ca_{1+y}Cu_{2+z}O_{8+\delta}$	2212
$Bi_{2+x}(Sr_{2-x-y}Ca_y)Cu_{1+z}O_{6+\delta}$; x = 0.1 to 0.4	2201-R
$(Sr_{14-x}Ca_x)Cu_{24}O_{41+\delta}$; x = 0 to 7[a]	$0\underline{14}\times\underline{24}$
$(Sr_{1-x}Ca_x)CuO_{2+\delta}$; x = 0 to 0.75	01×1
$(Sr_{2-x}Ca_x)CuO_{3+\delta}$; x = 0.0 to 2.0	02×1
$Bi_2(Sr_{3.9-x}Ca_x)O_{9-\delta}$; $x \cong$ 0.5 to 1.7[a]	24×0
$(Sr_{3-x}Ca_x)Al_2O_{6+\delta}$; x = 0.0 to 3.0[a]	$03\times Al_2$

[a]Sr:Ca ~ 2:1 typically observed in 2212 composition melt-processed films; x indicates (Sr,Ca) solid-solution.

TABLE II. Powder compositions tested.[a]

Powder	Precursor powder composition (molar basis; Al_2O_3 is nano-size)	Al_2O_3 addition (mass fraction)	Sr:Ca ratio	$(Sr_{3-x}Ca_x)Al_2O_6$ reaction product[b] (volume fraction, *n* mol)	Bi:Sr:Ca:Cu:O reaction product[b]
B1	$Bi_2Sr_2CaCu_2O_{8.2\pm\delta}$		2.0		
B1x	$Bi_2Sr_2CaCu_2O_{8.2+\delta}$ + 0.095 Al_2O_3	1.1%	2.0	$Sr_2CaAl_2O_6$ (6.6%, 0.10)	$Bi_2Sr_{1.81}Ca_{0.905}Cu_2O_{7.9+\delta}$
B2	$Bi_2Sr_{2.38}Ca_{1.15}Cu_{2.92}O_{9.7+\delta}$		2.07		
B2x	$Bi_2Sr_{2.38}Ca_{1.15}Cu_{2.92}O_{9.7+\delta}$ + 0.109 Al_2O_3	1.1%	2.07	$Sr_{2.02}Ca_{0.98}Al_2O_6$ (6.6%, 0.11)	$Bi_2Sr_{2.16}Ca_{1.04}Cu_{2.92}O_{9.4+\delta}$
B3	$Bi_{2.1}Sr_{2.0}Ca_{1.5}Cu_{2.0}O_{8.9+\delta}$		1.33		
B3x	$Bi_{2.1}Sr_{2.0}Ca_{1.5}Cu_{2.0}O_{8.9+\delta}$ + 0.2 Al_2O_3	2.1%	1.33	$Sr_{1.71}Ca_{1.29}Al_2O_6$ (12.6%, 0.2)	$Bi_{2.1}Sr_{1.66}Ca_{1.24}Cu_2O_{8.25+\delta}$ (B5 powder)
B4	$Bi_2Sr_{2.93}Ca_{1.46}Cu_2O_{9.6+\delta}$		2.0		
B4x	$Bi_2Sr_{2.93}Ca_{1.46}Cu_2O_{9.6+\delta}$ + 0.464 Al_2O_3	4.5%	2.0	$Sr_2CaAl_2O_6$ (25.0%, 0.46)	$Bi_2Sr_2CaCu_2O_{8.2+\delta}$ (B1 powder)
B5	$Bi_{2.1}Sr_{1.66}Ca_{1.24}Cu_2O_{8.25+\delta}$		1.33		

[a]x indicates powder with nano-size Al_2O_3 added.
[b]Assuming complete reaction of Al_2O_3 to form $(SrCa)_3Al_2O_6$.

suffix x) by mixing thoroughly with mortar and pestle. Also in Table II, powders B1 and B5 were prepared as nominal single-phase compositions, for comparison with results obtained with Al-containing composites (B1x, B2x, B3x, and B4x). In Table II, the initial Sr:Ca ratio of $(Sr,Ca)_3Al_2O_6$ and 2212 reaction products was assumed to be equal for calculating molar reactions. The oxygen contents of the powders in Table II were calculated using a Cu valence of +2.2, which closely approximates the oxygen content of 2212 quenched from approximately 850 °C.[30]

The relation of powder compositions in Table II to 2212 single-phase solid-solution regions in the Cu = 2 plane[31–35] is shown in Fig. 1. In Fig. 1, compositions B1 (≅B4x 2212 reaction product) and B5 (≅B3x 2212 reaction product) are in the Cu = 2 plane and are within or border on the single-phase region. These compositions were chosen for this study because of their possible use for wire fabrication and applications. The B5 composition forms much quicker and with higher purity in powder processing and may have similar advantages for wire fabrication.[34] Powders B3 and B4 were prepared so that molar reaction with nanophase Al_2O_3 would produce composites of $(Sr,Ca)_3Al_2O_6$ with the above-mentioned 2212 reaction products (B1 and B5). Powder B1x was chosen to study the effect of Al_2O_3 addition on the 2212 composition, similar to previous work.[15] Powder B2x has initial composition (2212 + 15% volume fraction $0\underline{14} \times \underline{24}$) and was studied to determine whether Al_2O_3 addition could increase and inhibit coarsening of the $0\underline{14} \times \underline{24}$ phase to enhance flux-pinning.[13] In Fig. 1, the (Al-free) 2212 reaction products of the composites from Table II are plotted, to demonstrate how reaction of Al_2O_3 with Bi-2212 type compositions moves the Bi–Sr–Ca–Cu–O reaction products in $BiO_{1.5}$–SrO–CaO–$Cu_2O_{4+\delta}$ phase space.

Thick-film tapes were made by adding approximately 30 mg of powder to approximately 0.5 ml of dehydrated alcohol and brush-coat depositing the resulting solution onto Ag foil (99.9% purity, 0.0050-cm thick). Powders were stored in a drybox with desiccant, to avoid long-term chemical reactions with solvents and moisture. The average film thickness was determined using the mass and area of the thick film and controlled from 13 to 17 μm to keep XRD film peak intensities consistent.

Figure 2 indicates the partial-melt processing profile used. In Fig. 2 only T_{max} was varied (shown with several examples) and the recrystallization using slow cooling from 856 to 847 °C[6,7] was held constant. The heating and cooling rates to/from approximately 845 °C are

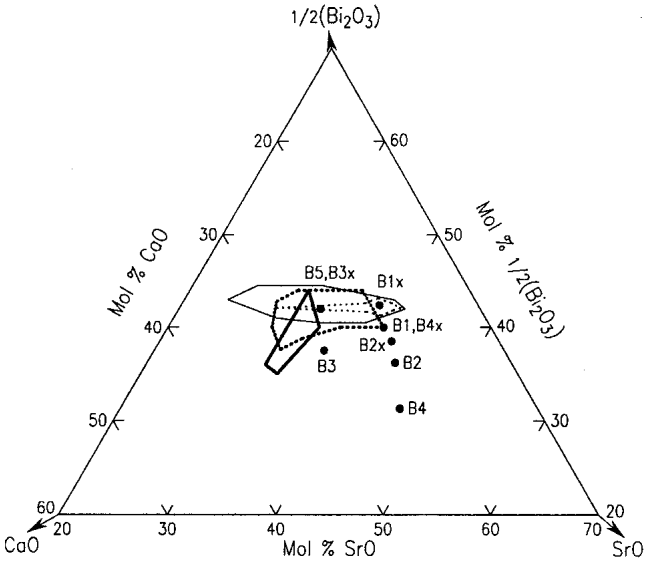

FIG. 1. Bi–Sr–Ca–Cu–O compositions in the Cu = 2 plane tested in this study before reaction (B1 to B5) and Bi–Sr–Ca–Cu–O products after reaction with Al_2O_3 (B1x to B4x), from Table II. Lines indicate outer boundaries of single-phase regions at 800 to 850 °C of solid-solution Bi-2212 by (···) Majewski[31] in agreement with Knížek *et al.*,[35] (—) Muller *et al.*,[33] (—) Holesinger *et al.*,[32] and (···) Sinclair.[34] With subscripts normalized to 7, powders are in the Cu = 2 plane except B1x (Cu = 2.08), B2 (Cu = 2.42), B2x (Cu = 2.51), B3 (Cu = 1.84), and B4 (Cu = 1.67).

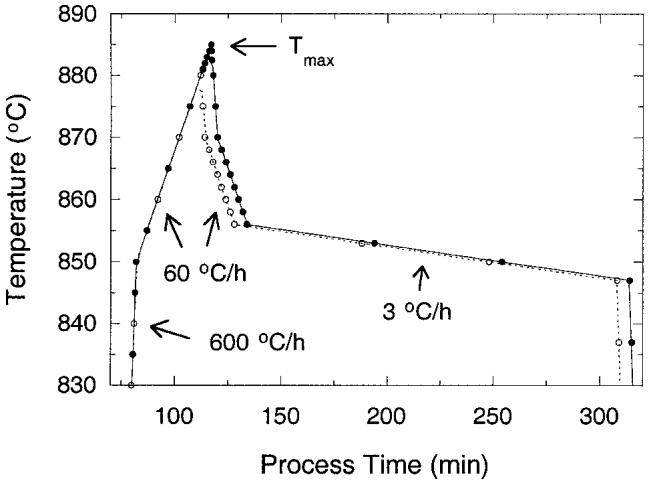

FIG. 2. Partial-melt growth temperature–time process profile, showing examples for different maximum process temperatures (T_{max}) = 885 °C (●) and 880 °C (○). The cooling rate from 870 to 856 °C is 300 °C/h.

comparable to rates that can be achieved with large-scale processing furnaces. The cooling rate below 847 °C was furnace cooling in the power-off mode: from 847 to 500 °C at about 600 to 120 °C/h and from 500 to 40 °C at about 120 to 60 °C/h, decreasing in cooling rate as the oven temperature decreased.

XRD data were obtained with a Philips (Eindhoven, The Netherlands) diffractometer equipped with 12-mm optics, incident Soller slits, and a θ compensating slit with graphite monochromator and automated with the use of Radix Databox interfaces. The 2θ peak positions reported here were externally calibrated using SRM 660 LaB_6[36] as a reference. Data were collected using Cu K_α radiation with a 2θ step size of 0.03 Å and a 1.8-s count time. Peak-intensity data were determined as relative peak heights above background using the Siemens DIFFRAC5000 (Karlsruhe, Germany) s derivative peak location program. The standard error in peak-intensity measurements from experimental factors was <5%.

The texture of the 2212 tapes was analyzed using a technique in which an ω-scan was recorded using a powder x-ray diffractometer and corrected for defocus and absorption.[37–40] The measurements were performed with a Siemens D500 (Karlsruhe, Germany) powder x-ray diffractometer equipped with an incident beam Ge monochromator tuned to only transmit Cu $K_{\alpha 1}$ radiation. The 00$\underline{2}$0 Bragg peak was used for the ω-scan, and the absorption and defocus corrections using the profile of the 00$\underline{2}$0 peak were applied to the ω-scan data as described previously,[37,38] using the software package TexturePlus.[39] For the background, ω-scans were obtained at a 2θ value 2° above the 00$\underline{2}$0 peak. Two measures to characterize the texture were obtained, the full width half-maximum (FWHM) of the corrected ω-scan and the integrals of the corrected ω-scan calculated as $\int I(\omega) \sin(\omega)\, d\omega$.[40] The FWHM is a measure of how sharply the textured material is oriented. The ω-scan integral can be used to measure the volume fraction of material that is textured.[40] Another measure of texture, the texture factor, was measured from the θ–2θ scans as $F_T = F/F_o$, where $F = \{\Sigma I_{c\ axis}/\Sigma(I_{c\ axis} + I_{powd})\}$, $I_{c\ axis}$ are intensities of the *c*-axis-oriented peaks (002 and 00$\underline{16}$), I_{powd} are intensities of non-*c*-axis-oriented peaks (113 and 200), and F_o is the value of F for the PDF reference powder patterns.[28,41–43] The texture factor is a semiquantitative, comparative measure of the volume fraction of textured material.

Energy dispersive x-ray spectrometry (EDS) was used to acquire compositional data using conventional methods, with data reduction via the DeskTop Spectrum Analyzer (DTSA) software package.[29,44] Standards for EDS analysis were $Bi_2Sr_{1.5}Ca_{1.5}Cu_2O_x$ and corundum.

Superconducting properties of films and powders were measured with a superconducting quantum interference device (SQUID) magnetometer (Quantum Design, MPMS/MPMS^2) (San Diego, CA), which cools the samples with a cryocooler and measures the magnetization–applied field (*M–H*) loops in a low vacuum. To characterize films, rectangularly shaped samples about 3.2-mm square were placed in low magnetic response organic sample holders with the tape surface oriented perpendicular to the applied magnetic field. *M–H* hysteresis loops at different temperatures were made by heating samples to 100 K and zero-field cooling (ZFC) to the measurement temperature. The magnetic J_c of films was estimated using the extended Bean critical current model $J_c = 20(\Delta M)3b/[a(1 - a)]$, where ΔM is the magnetic hysteresis difference, and a and b are the dimensions of the sample cross section perpendicular to the applied magnetic field.[45] The ΔM values for positive and negative applied magnetic fields were compared to find the error of measurement.

To characterize the superconducting properties of powders, field-cooled (FC) Meissner and ZFC measurements were performed from 5 to 125 K.[46] The SQUID magnet was reset to zero before any measurements. The superconducting volume fractions were calculated using $\chi = 4\pi\chi_v/(1 - D^*4\pi\chi_v)$, where $\chi_v = M/H_{appl}$ is the measured magnetic susceptibility, and $D = 0.3333$ is the demagnetization factor assuming a spherical particle distribution.[6,46] The applied magnetic field was $H_{appl} = 796$ A/m $- H_{rem}$, where H_{rem} is the remnant field of the magnet after resetting to zero, determined for each sample by measuring $M(H)$ from 796 A/m to –398 A/m at 79.6 A/m intervals and plotting when $M = 0$ (±7.96 A/m accuracy).

Temperatures used for processing were measured at the sample position with S-type thermocouples calibrated with gold melting (approximately 2 °C standard uncertainty). The volume densities used in this

work were $Bi_2Sr_2CaCu_2O_{8+\delta}$ = 6.60 g/cm^3 [6,47] and $Bi_{2.1}Sr_{1.66}Ca_{1.24}Cu_2O_{8+\delta}$ = 6.63 g/cm^3.[35] The density of $Sr_{3-x}Ca_xAl_2O_6$ was calculated for different Ca content (x) using a polynomial equation fit of Rietveld XRD density measurements of powder samples prepared with Ca = 1.0 to 2.0, $\rho = 4.0894 - 0.179x - 0.084364x^2$ for x Ca content.[16] The densities for $(Sr,Ca)_3Al_2O_6$ are in good agreement (<0.2%) with values by Walz.[48]

The Ca content of $(Sr,Ca)_3Al_2O_6$ in films was determined by measuring the 2θ shift of the 440 peak and comparing to the 2θ shift for bulk compositions as plotted in Fig. 3. The linear fits in Fig. 3 were used for determining the Ca content of films. The varying slopes of the linear fits for Ca < 1.0 and Ca > 1.0 suggest that different ordering in the phase may be occurring. Bulk powders of $(Sr,Ca)_3Al_2O_6$ in Fig. 3 were prepared by the solid-state method using a final sinter temperature of 1275 to 1325 °C.[16]

III. RESULTS AND DISCUSSION

A. Bi–Sr–Ca–Cu–Al–O phase formation and assemblages

The primary phases that formed in the films were determined by XRD patterns, as shown in Figs. 4(a) and 4(b) for films with Al_2O_3 added (compositions ending with suffix x), and compared to reference films made from single-phase compositions (B1 and B5). All of the major XRD peaks in Fig. 4 could be identified using the phases given in Table I. The identification of all XRD peaks suggests the volume fraction of unknown Bi–Sr–Ca–Cu–Al–O phases, if they exist, is <3–5%.[49] The highest intensity XRD peaks of $(Sr,Ca)_3Al_2O_6$ {440, 444 and 800 and 844}[47] were always observed with strong intensity in melt-processed films with Al_2O_3 added. In particular, the 440 and 800 peaks can be clearly discerned in Fig. 4 for all films with Al_2O_3 added (compositions ending with suffix x).

Figures 5(a)–5(d) plot the assemblage and formation of major phases in different composition films fully processed as a function of T_{max} temperature, as measured by XRD peak intensities. In Fig. 5, the absolute peak intensity for unique and high-intensity *hkl* lines are plotted, which are representative of the relative volume fraction of the preferred orientations of phases formed: the 008 peak of 2212 is a measure of the amount of *c*-axis-oriented phase, the 110 peak of 01 × 1 and 040 peak of 0$\underline{1}$4 × $\underline{2}$4 represent the intensity of the *ab*0-oriented phase, the 101 peak of 02 × 1 gives the intensity of *a*0*c* orientation, and the 440 peak of 03 × Al_2 represents the intensity of the random-oriented phase. The *hkl* lines chosen can be observed in Fig. 4. The intensities of these orientations are a good measure of the phase formation as

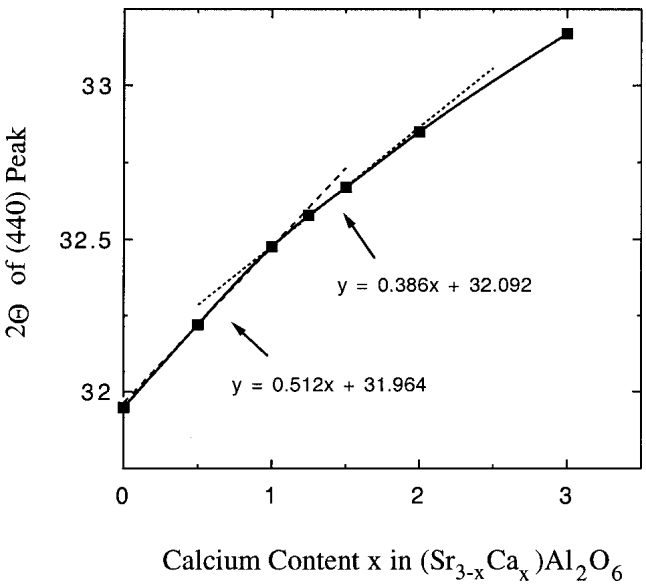

FIG. 3. Two-theta shift of the 440 peak of $(Sr,Ca)_3Al_2O_6$ powders processed at 1275 to 1325 °C, for different Ca content. Two-theta for end members are from PDF cards (Nos. 24-1187 and 28-1429).[28] Standard errors of measurements for 2θ were too small (<0.03°) to be seen in the figure.

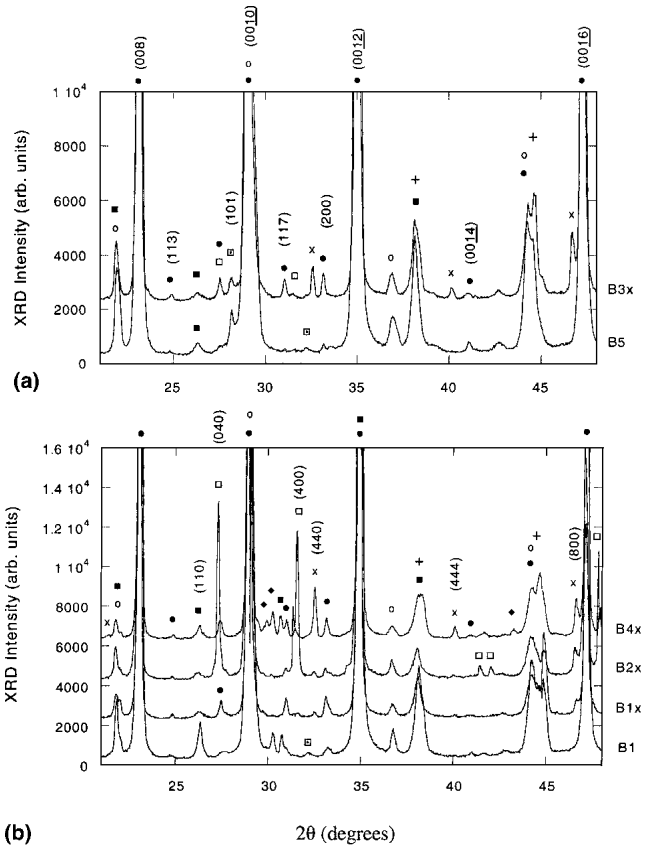

FIG. 4. XRD patterns of films processed with T_{max} = 880 °C profile with different reference compositions: (a) B1; (b) B5. Phases observed include: (●) 2212; (○) 2201; (■) 01 × 1; (◆) 24 × 0; (×) 03 × Al_2; (□) 0$\underline{1}$4 × $\underline{2}$4; (▣) 02 × 1; (+) Ag substrate or Al holder. Significant (*hkl*) peaks are labeled.

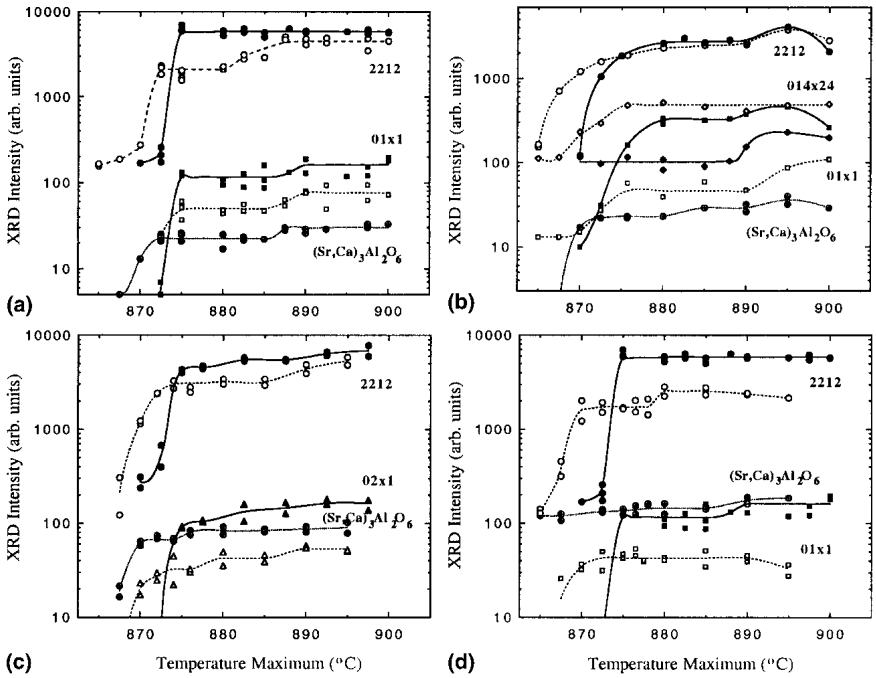

FIG. 5. Phase formation and assemblages measured by selected XRD peak integrated intensity measurements as a function of maximum process temperature (T_{max}) for Al_2O_3 addition and Al_2O_3-free reference films: (a) B1x (light symbols) with B1 reference (solid symbols); (b) B2x (light symbols) with B2 reference (solid symbols); (c) B3x (light symbols) with B5 reference (solid symbols); (d) B4x (light symbols) with B1 reference (solid symbols). The *hkl* indices of peaks plotted were 008 for *c*-axis-oriented 2212, 110 of *ab*0-oriented 01 × 1, 040 peak of *ab*0-oriented $0\underline{14} \times \underline{24}$, 101 of *a*0*c*-oriented 02 × 1, and 440 of random-oriented 03 × Al_2.

a whole, as only very small XRD peak intensities of other orientations were observed for these phases, as seen in Fig. 4.

The formation of high-intensity *c*-axis-textured 2212 phase in Figs. 5(a)–5(d) occurred in films that underwent a meltinglike transition, which was observed visually in real time as a quick darkening of the film. This observation is consistent with previous work.[6] Figures 5(a)–5(d) indicate that strong formation of $(Sr,Ca)_3Al_2O_6$ was observed in films when T_{max} just reached or was slightly below the melting threshold; i.e., when T_{max} was high enough to allow formation of *c*-axis-oriented 2212 phase.[6] The difference between films with neglible $(Sr,Ca)_3Al_2O_6$ phase intensity and almost maximum intensity was only a few degrees increase of T_{max} corresponding to an additional few minutes of melting [Fig. 5(c) for example]. One exception to this trend, however, was for B4x powder, where $(Sr,Ca)_3Al_2O_x$ formation occurred at $T_{max} < 865$ °C without formation of textured 2212 phase and during the approximately 4-h anneal and recrystallization process. We speculate that a small amount of liquid formed for this composition at temperatures < 865 °C because of the increased Ca and Cu content that accelerated formation of $(Sr,Ca)_3Al_2O_6$ without the formation of textured 2212 phase. A small increase in $(Sr,Ca)_3Al_2O_6$ intensity was also observed at approximately 885 to 895 °C for several of the powders (B1x and B4x), suggesting more complete formation of $(Sr,Ca)_3Al_2O_6$ for these compositions at higher T_{max} process profiles. In contrast for B3x powder, $(Sr,Ca)_3Al_2O_6$ formation reached a maximum simultaneously with formation of (nearly) maximum textured 2212 phase.

Figures 5(a)–5(d) indicate that Al_2O_3 addition significantly reduced Sr–Ca–Cu–O phase defect volume fractions by factors of approximately 2 to 6. For example in Fig. 5(a) for B1x composition, Al_2O_3 addition reduced 01 × 1 formation by a factor of 2. For B3x composition in Fig. 5(c), 02 × 1 formation was reduced by factors of 2 to 4 with addition of approximately 13% volume fraction of 03 × Al_2 phase (by composite reaction). For B2x composition, Al_2O_3 addition reduced 01 × 1 formation by a factor of 6 and increased $0\underline{14} \times \underline{24}$ formation by factor of about 4 for T_{max} = 880 to 890 °C. The shift toward 014 × 24 formation in B2x powder is closer to the equilibrium phase assemblage expected, as the powder originally had composition ($Bi_2Sr_2CaCu_2O_{8+\delta}$ + 15% volume fraction $Sr_{10}Ca_4Cu_{24}O_x$).[14]

The trend for reducing Sr–Ca–Cu–O defect formation with addition of nanophase Al_2O_3 was also observed in scanning electron microscopy (SEM) images, as shown in Figs. 6–8 for different magnifications and varying T_{max} temperatures. As an example, Figs. 6–8 show the dramatic decrease of 02 × 1 defect size and volume fraction in B5 composition films after addition of approximately 13% volume fraction $(Sr,Ca)_3Al_2O_6$ particles (by

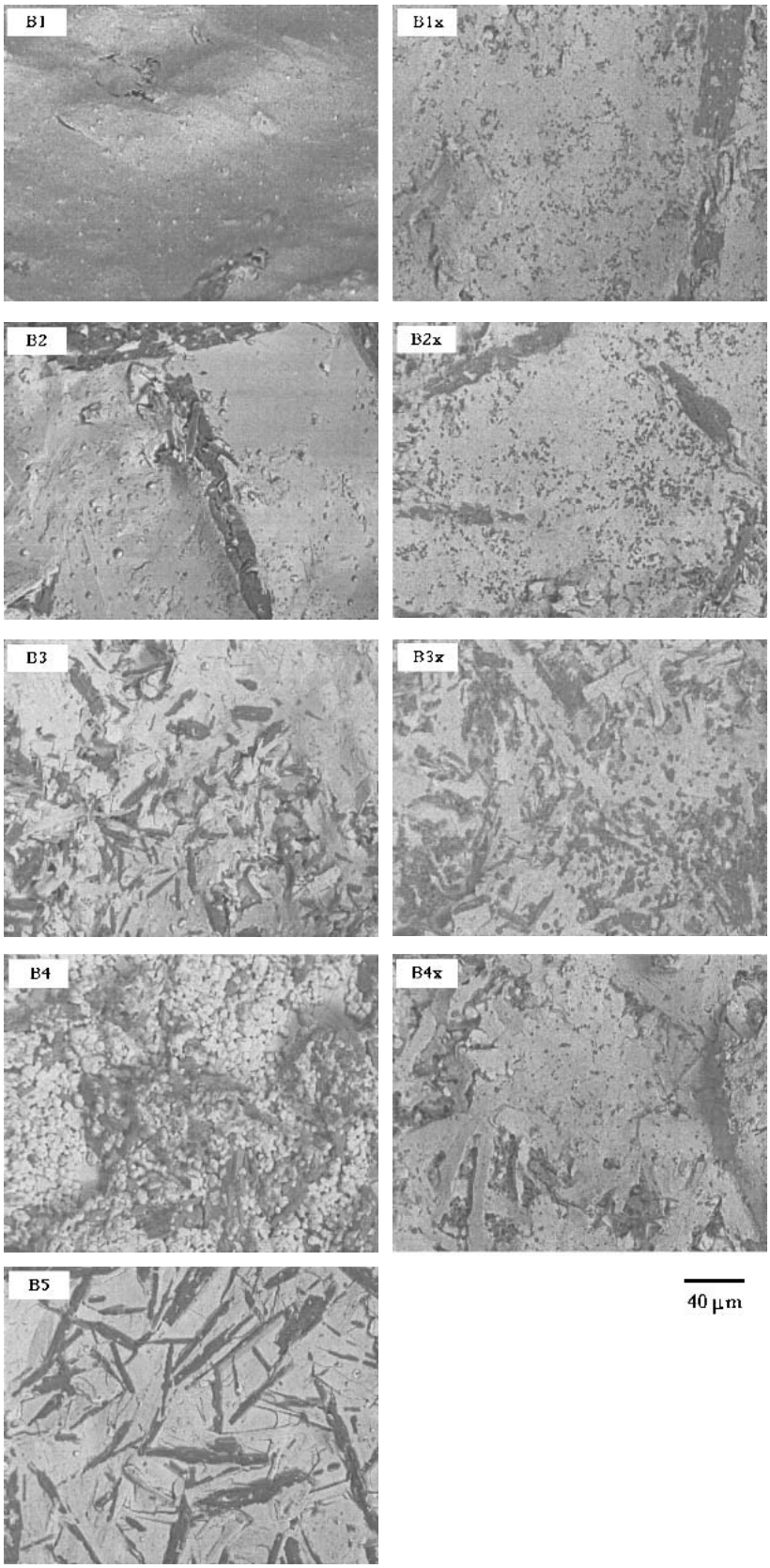

FIG. 6. Backscattered SEM images of films processed with T_{max} = 880 °C profile. Large dark-color needles or defects in B1, B1x, B2, and B2x films are 01 × 1 or 0$\underline{14}$ × $\underline{24}$ defects. Micron-sized (dark approximately round) defects in B1x, B2x, B3x, and B4x films are 03 × Al_2. Needle defects for B3x and B5 films are $(Sr_{0.2}Ca_{1.8})CuO_x$.

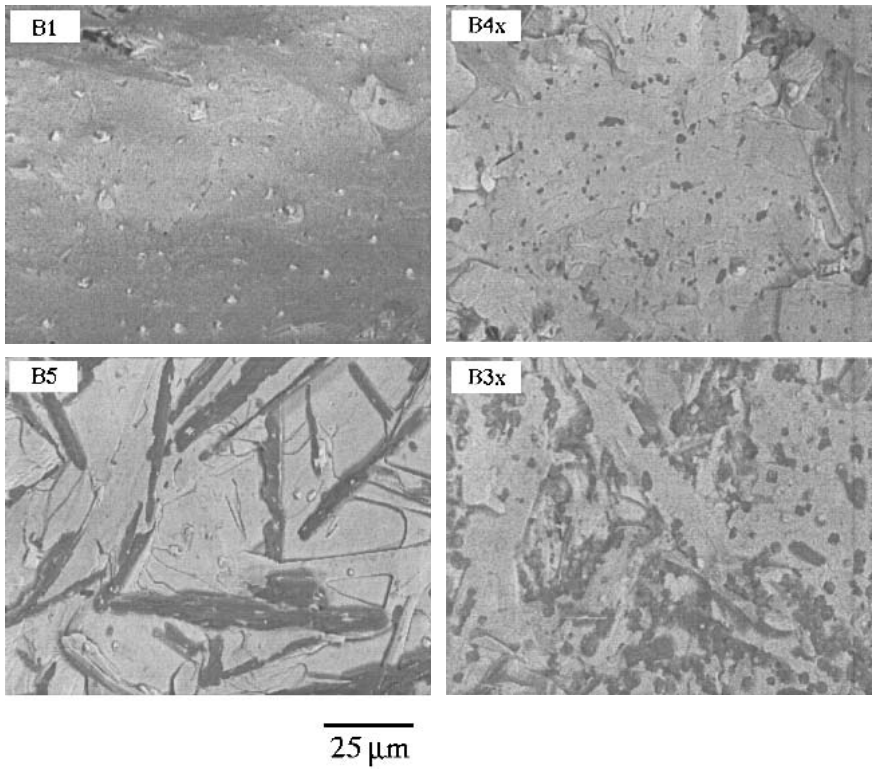

FIG. 7. Backscattered SEM images from Fig. 6 at higher magnification, showing formation of O3 × Al_2 defects (dark round-shaped) for B3x and B4x and reduction of $(Sr,Ca)_2CuO_x$ defects (dark needle-shaped) with 03 × Al_2 addition (B5 compared to B3x). B1 and B5 films have approximate composition of 2212 regions in B4x and B3x films, respectively.

composite reaction) for B3x composition films. The ~(2–4)-fold decrease of 02 × 1 defects with addition of $(Sr,Ca)_3Al_2O_6$ particles seen in SEM images correlates with the decrease measured by XRD intensities for a range of T_{max} temperatures [Fig. 5(c)]. The reduction and refinement of second-phase defects with Al_2O_3 addition for a large range of process temperature is consistent with previous results for isothermal processing of Bi-2212.[15]

B. Bi-2212 texturing and $(Sr,Ca)_3Al_2O_6$ defect coarsening

The addition of nanophase Al_2O_3 had only a small effect on *c*-axis texturing of the 2212 phase, as determined by SEM, XRD peak intensity measurements, and XRD ω-scans. The FWHM of corrected ω-scans from a variety of thick films processed with and without addition of Al_2O_3 were all in the range of 8° to 11°, indicating the sharpness of the texture of the *c*-axis 2212 phase was not significantly affected by Al_2O_3 addition. However the integral of the 00$\underline{2}$0 peak ω-scans, normalized to a 2212 volume fraction of unity, showed a decrease of approximately 25% as the $(Sr,Ca)_3Al_2O_6$, fraction increased to approximately 25% as indicated in Fig. 9. This shows that the volume fraction of *c*-axis-oriented 2212 phase in this material was significantly reduced, but what remains has the same degree of texture.

SEM images confirmed the trends observed with x-ray texture measurements. The 2212 textured areas in Figs. 6–8 were smooth in most of the areas where clustered defects were not observed, which indicates the 2212 phase is highly oriented in general, while remaining in metallurgical contact with nonclustered $(Sr,Ca)_3Al_2O_6$ particles. Careful analysis of film surfaces and polished cross sections by SEM suggest that disruption of *c*-axis texturing occurred mostly in areas surrounding clustered $(Sr,Ca)_3Al_2O_6$ defects rather than around individual $(Sr,Ca)_3Al_2O_6$ defects. Inside the 2212 layers, the $(Sr,Ca)_3Al_2O_6$ defects were uniformly distributed and with the same size distribution, as indicated by SEM cross sections.

XRD powder diffraction also confirmed the trends observed with SEM and ω-scans. The 2212-textured peak intensities in Fig. 5 for B1x, B2x, and B3x powders showed almost no decrease in intensity with $(Sr,Ca)_3Al_2O_6$ volume fraction additions compared to B1 and B5 reference films, after accounting for differences in 2212 volume fraction changes and $(Sr,Ca)_3Al_2O_6$ additions (Table II; intensities in Fig. 5 were plotted as raw values). After normalizing, the 2212 intensities in Fig. 5 showed only a small decrease in intensity with addition of $(Sr,Ca)_3Al_2O_6$ particles. This is in sharp contrast to the effect that was observed with Au nanoparticle addition to Bi-2212 (for example).[13] Regardless of the processing

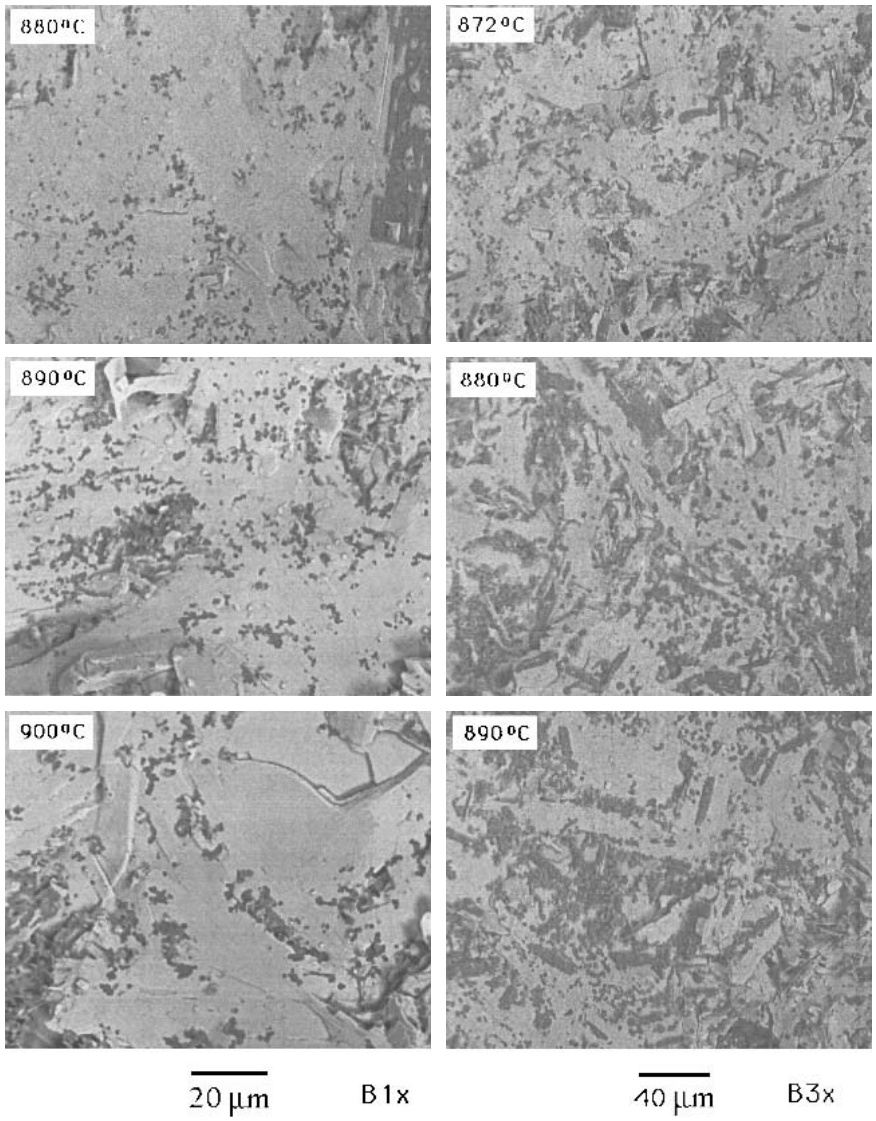

FIG. 8. Backscattered SEM images of B1x and B3x films indicate coarsening of 03 × Al_2 defects with increasing T_{max} process temperatures (in box inserts). The 03 × Al_2 defects are dark color and round-shaped.

conditions attempted, *c*-axis texturing was completely disrupted with the addition of Au nanoparticles.[13] However when Au was used as a substrate material, Au did not disrupt *c*-axis texturing or 2212 phase formation.[50] These results, combined with previous experience with Sr–Ca–Cu–O defects[16] and work on MgO,[12] suggest that, by comparison, oxide defects may in general have a minimal effect on *c*-axis texturing during 2212 partial-melt processing. This would be an important determination and consideration, as *c*-axis texturing is a necessary prerequisite to obtain high transport J_c in Bi-2212 conductors.[4,5]

While the sharpness of the *c*-axis texturing was not significantly affected by addition of Al_2O_3 [and subsequent formation of $(Sr,Ca)_3Al_2O_6$], a small increase in the intensity of the non-*c*-axis-oriented peaks of 2212 (113 and 200) was always observed in the XRD patterns (Fig. 4). The increase of non-*c*-axis peak intensities has an effect on the *F* factor, as plotted in Fig. 9 for varying addition of Al_2O_3. For all cases of Al_2O_3 addition, the *F* factor dropped from approximately 0.97 to 0.92. However this decrease was not large, considering the amount of defect addition (up to 25% volume fraction). It is speculated that the small observed increase of the non-*c*-axis peak intensities could be due to 2212 platelets that are misoriented in areas surrounding clustered $(Sr,Ca)_3Al_2O_6$ particles, as discussed above (i.e., Al_2O_3 addition slightly increased the randomly oriented population of the 2212 phase).

The images in Fig. 8 show how particles of $(Sr,Ca)_3Al_2O_6$ increased in size (coarsened) as the value for T_{max} was raised; e.g., from 872 and 890 °C. In general, the particles ranged from about 0.2 to 2 μm in size, varying with processing temperature and composition. The increase in particle size is expected to reduce the

number of pinning sites and consequently reduce the overall flux-pinning effect.[2] Therefore, the problem of defect coarsening would need to be considered in further optimization studies of this composite system.

C. $(Sr,Ca)_3Al_2O_6$ composition

The composition of the $(Sr,Ca)_3Al_2O_6$ defects in the films as measured both by EDS and XRD was in good agreement. The non-BiSrCaCuO-related XRD peaks in Fig. 4 for powders with Al_2O_3 addition correlated precisely with the XRD peaks of bulk $(Sr,Ca)_3Al_2O_6$, after accounting for the shift of the peaks with changing Sr:Ca ratio composition. The shift of the 440 peak and the Ca composition of $(Sr,Ca)_3Al_2O_6$ in processed films as measured by XRD is given in Table III. The Ca composition was determined using the $2\Theta_{avg}$ shift of the 440 peak, together with calibration curves in Fig. 3. The results in Table III indicate that the Ca content of $(Sr,Ca)_3Al_2O_6$ closely approximated that of the precursor powder (from 0–6% mole fraction difference). This is similar to what was observed for $(Sr_{9.3}Ca_{5.4})Cu_{24}O_x$ and 24 × 0 phases in B2x and B4x films, where the Sr:Ca ratio was approximately 2:1 and approximately equal to the Sr:Ca ratio of the precursor powder.

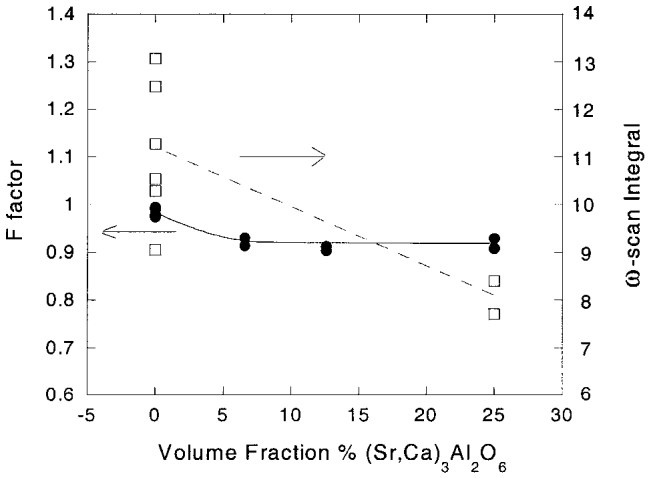

FIG. 9. *F* texture factor and ω-scan integral (normalized for 2212 phase volume fraction) for different volume fraction of $(Sr,Ca)_3Al_2O_6$ (0% = B1 or B5; 7% = B1x or B2x; 13% = B3x; 25% = B4x). Films were processed with T_{max} = 880 °C profile.

A small difference in Ca content of $(Sr,Ca)_3Al_2O_6$ in films versus Ca content in the precursor was noted in Table III among the compositions B1x, B2x, and B3x (approximately 4% to 6% mole fraction difference). However, this trend could be expected to some degree, as a significant amount of Sr–Ca–Cu–O defects (>5% volume fraction) was still present in the composite films, which could shift the Sr:Ca ratio of the Bi–Sr–Ca–Cu–O component during melt-processing. From semiquantitative analysis of defect volume fractions measured by XRD and SEM (Figs. 5–8), a general trend is suggested that as the volume fraction of $(Sr,Ca)_3Al_2O_6$ particles was increased, the amount of Bi–Sr–Ca–Cu–O defects decreased and the Sr:Ca ratio of $(Sr,Ca)_3Al_2O_6$ more closely approximated that of the precursor powder. The peak of this trend is seen for B4x composition, in which 25% volume fraction of $(Sr,Ca)_3Al_2O_6$ was added to 2212 composition powder (by reaction). This addition nearly eliminated the volume fraction of Sr–Ca–Cu–O defects in the film, and the Ca content of the $(Sr,Ca)_3Al_2O_6$ phase was almost exactly the same as the precursor powder (Ca = 1.00 for Sr + Ca content normalized to 3). Presumably, the Ca content of the 2212 reactant product was also closer to the ideal (Ca = 1.0) from mass balance considerations; however, this was not verified.

The T_{max} process temperature dependence of the Ca content of $(Sr,Ca)_3Al_2O_6$ was also reported in Table III. This variable would be important to consider for scaled up fabrication and processing of long lengths, where temperature variations are difficult to control.[7] Table III indicates that the Ca content of $(Sr,Ca)_3Al_2O_6$ was stable for a wide range of T_{max} temperatures, approximately 865 to 890 °C, with the exact temperature range varying depending on powder composition.

EDS measurement of $(Sr,Ca)_3Al_2O_6$ particles always showed a small amount of Bi and Cu in the composition. The mole fraction of Bi and Cu was in the range of 2–4%, which increased from approximately 2 to 4% as the particle size reduced in size from approximately 5 to 1 μm. The size dependence of this measurement can indicate that the 2212 matrix surrounding the $(Sr,Ca)_3Al_2O_6$ particles is fluorescing during EDS analysis.[29] When the 2212 matrix was subtracted out of the

TABLE III. Ca content of $(Sr_{3-x}Ca_x)Al_2O_{6+\delta}$ in films determined by XRD peak shift, compared to Ca content of precursor powder; (Sr + Ca normalized to 3 for precursor powders).

Precursor powder	Volume fraction of $(Sr,Ca)_3Al_2O_6$ (calculated[a])	$2\theta_{avg}$ of 440 peak of $(Sr_{3-x}Ca_x)Al_2O_6$ in films (deg)	T_{max} range evaluated (°C)	Ca_{avg} content (x) of $(Sr_{3-x}Ca_x)Al_2O_6$ by XRD	Ca content (x) of precursor powder
B1x	6.6%	32.445 ± 0.009	872 to 890	0.94 ± 0.02	1.00
B2x	6.6%	32.445 ± 0.007	870 to 895	0.94 ± 0.01	0.98
B3x	12.6%	32.571 ± 0.009	870 to 890	1.24 ± 0.02	1.29
B4x	25%	32.483 ± 0.004	865 to 895	1.01 ± 0.01	1.00

[a]Assuming complete reaction of Al_2O_3 to form $(Sr,Ca)_3Al_2O_6$.

EDS measurements of $(Sr,Ca)_3Al_2O_6$, the remaining compositions almost exactly matched the compositions of $(Sr,Ca)_3Al_2O_6$ measured with XRD [e.g., a $(Sr,Ca)_{0.61}Al_{0.39}O_x$ composition was measured for Al-containing particles in B2x powder, in agreement with XRD measurements].

D. Superconducting properties of [Bi-2212 + *n*$(Sr,Ca)Al_2O_3$] composite films

The superconducting properties of B3x and B4x composite films are shown in Table IV, compared to nominal single-phase reference films (B5 and B1) with compositions equal to the expected Bi–Sr–Ca–Cu–O reactants of B3x and B4x (Table II). After melt processing and formation of $(Sr,Ca)_3Al_2O_6$, there was slight degradation of superconducting properties for B3x and B4x, compared to their respective reference films. The critical temperature (T_c) decreased slightly by about 3 K for both B3x and B4x films, compared to B1 and B5 reference films. This correlates very closely with the decrease in T_c measured for B1-type bulk composites with the exact same composition: a 2–4 K decrease of T_c was measured for bulk composites of $\{Bi_2Sr_2CaCa_2O_{8+\delta}$ + (0–24%) volume fraction of $Sr_2CaAl_2O_6\}$ sintered for over 500 h at 860 °C.[16] The decrease of T_c could occur from very slight solubility of Al into the Bi-2212 matrix ($\leqslant$0.1 Al concentration/formula unit),[22] a possibly different Bi:Sr:Ca cation intersubstitution in the lattice, or small composition variations from the different reaction paths.[16]

Table IV also gives the ZFC and FC volume fractions and magnetic J_cs for B3x, B4x films, and reference films. For B3x composition films, there was no significant change of these superconducting properties compared to B5 reference films. For B4x powders, however, there was a measurable decrease in ZFC and FC volume fractions to 60% of the reference (B1). The decrease in volume fractions for B4x composition is consistent with XRD peak intensity data (Fig. 5), which showed a drop to approximately 60% of the B1 reference intensity (after normalizing for superconducting volume fractions). For B4x composition, however, the decrease in film J_c was not significant when compared to a reference film (B1). The reason for the decrease of ZFC and XRD volume fractions for B4x films is unknown at present; however, the drop suggests the reaction was not complete for the processing parameters chosen. A higher T_{max} temperature might have allowed more complete formation of 03 × Al_2, as suggested in Fig. 5(d). As discussed above, $Bi_2Sr_2CaCu_2O_{8+\delta}$ and $Sr_2CaAl_2O_6$ compositions are chemically stable with each other at 860 °C;[16] therefore, a different reaction route (e.g., melt processing of Bi-2212 powder and $Sr_2CaAl_2O_3$ nanoparticles) also might be considered to process these composites to achieve higher superconducting volume fractions.

The effect of $(Sr,Ca)_3Al_2O_6$ formation on flux pinning properties is shown in Figs. 10 and 11, where the increase in magnetic J_c is plotted for different applied fields and different volume fraction of $(Sr,Ca)_3Al_2O_6$, and compared to values achieved for (Bi,Pb)2212 crystals,[51,52] 2212 single-phase film,[11,53] and an irradiated single-phase film.[11] In Figs. 10 and 11 normalized $J_c(T)$ curves were compared, as zero-field J_cs varied significantly depending on the type of sample (crystal or film) and the amount of processing optimization. However, normalized $J_c(T)$ curves were found to be consistent for a range of J_c; e.g., J_c(5 K, 0 T) values from 34,000 to 82,000 A/cm^2 gave the same normalized $J_c(T)$ curves in Fig. 10 for B3x powders. Plots in Fig. 10 for $(Sr,Ca)_3Al_2O_6$ addition were average values from measurements of two different films processed by the same conditions, so the improvement of flux pinning was consistent. With increasing addition of $(Sr,Ca)_3Al_2O_6$ defects, a significant increase in normalized (and by calculation absolute) J_c was observed at 20–30 K and 0–2 T applied field. For 25% volume fraction addition, nearly one order of magnitude improvement of normalized J_c was achieved at 20 K compared to single-phase 2212 films, and at 30 K the improvement in J_c was even greater and close to that achieved with (Bi,Pb)2212 single crystals.[51,52] Further improvements in flux pinning are required, however, to reach the values achieved by irradiation.[11]

An important point to consider is whether Al is contributing to flux pinning by substituting into the 2212 crystal structure, for example on the Cu lattice

TABLE IV. Superconducting properties of films processed with T_{max} = 880 °C. The zero-field-cooled (ZFC) and field-cooled (FC) volume fractions and T_c were measured on (powdered) films. J_c was measured for rectangular films.

Composition[a]	T_c (K) (±0.5 K)	ZFC volume fraction @ 5 K and 976 A/m (±5%)	FC volume fraction @ 5 K and 976 A/m (±5%)	J_c (A/cm^2)[b] at 5 K, 0 T (±10%)
B1	80	87%	58%	38,000
B4x ≅ B1 + 25% 03 × Al_2	77	51%	37%	39,000
B5	83	78%	57%	60,000
B3x ≅ B5 + 13% O3 × Al_2	80	74%	51%	64,000

[a]03 × Al_2 are volume fractions; assuming complete reaction of Al_2O_3 to form $(Sr,Ca)_3Al_2O_x$ as shown in Table II.
[b]Calculated using superconducting volume fraction.

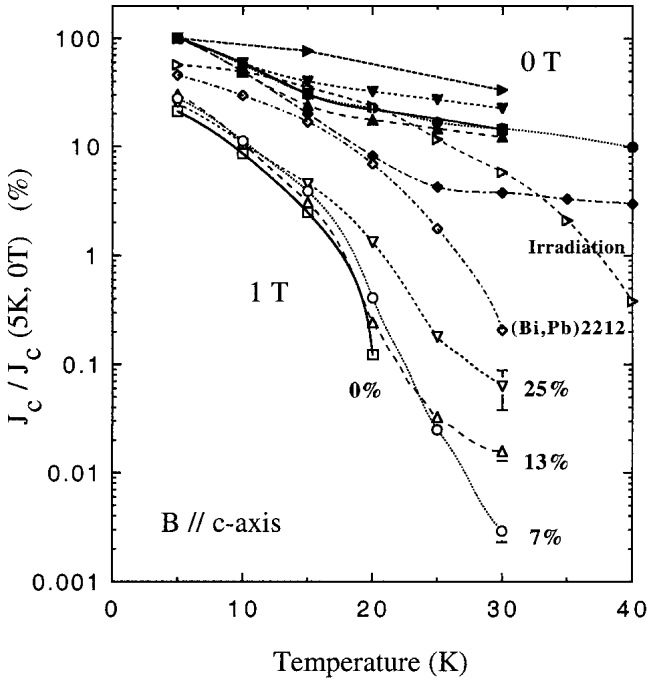

FIG. 10. Magnetic J_c as a function of temperature for H_{appl} = 0 T (dark symbols) and 1 T (light symbols). J_cs were normalized by the respective zero-field values at 5 K; J_c(5 K, 0 T) = 105,000 (0%).[11] 33,000 (7% = B2x), 34,000 to 82,000 (13% = B3x), 39,000 (25% = B4x), 10^6 (Bi,Pb crystal),[51,52] and 145,000 (irradated tape).[11] Error bars indicate standard errors from two (or more) measurements. Magnetic field was applied parallel to *c*-axis direction (perpendicular to tape surface). Values at 1 T for the (Bi,Pb)crystal were extrapolated from published $J_c(H)$ curves up to 0.9 T.[51,52]

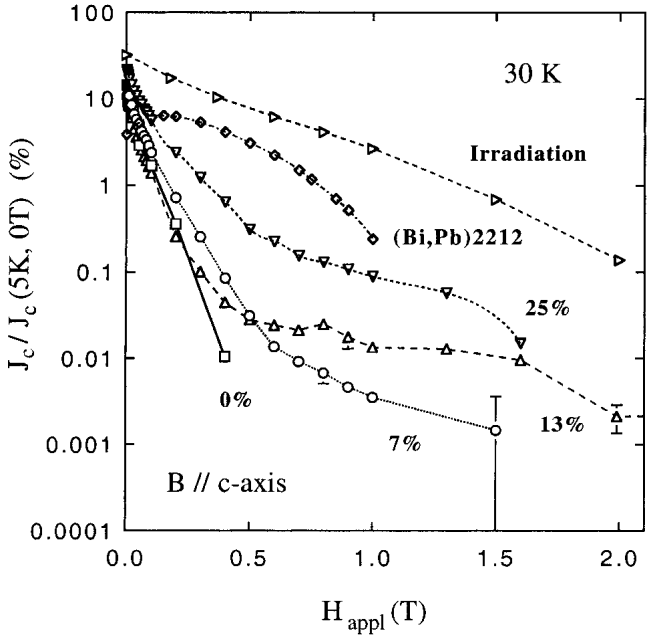

FIG. 11. Normalized magnetic J_c at 30 K of samples in Fig. 10. Error bars indicate standard errors from two measurements.

sites. However, there was little evidence to support this possibility. EDS measurements in defect-free areas did not show detectable Al content in agreement with previous work,[15] and EDS element mapping images showed Al only located in $(Sr,Ca)_3Al_2O_6$ defects. The superconducting properties of the films in Table IV showed only slight degradation of T_c and, for B3x composition, no reduction of other superconducting properties.

IV. CONCLUSIONS

The addition of essentially chemically inert submicron- to micron-sized $(Sr,Ca)_3Al_2O_6$ defects to varying composition solid-solution Bi-2212 conductors (formed by chemical reaction between Bi-2212 and Al_2O_3) was determined to be a method of reducing second-phase Sr–Ca–Cu–O defect formations in this material that is relatively insensitive to process temperature. Addition of $(Sr,Ca)_3Al_2O_6$ significantly enhanced flux pinning and caused only a small decrease in textured fraction of the 2212 phase for most compositions. The small effect on texturing is consistent with results in the literature for addition of oxide defects.

After partial-melt processing of {nanophase Al_2O_3 + Bi-2212-type} composite thick films, the primary Al oxide containing phase observed to form from the chemical reaction was solid-solution $(Sr,Ca)_3Al_2O_3$, with Sr:Ca ratio close or equal to that of the precursor powder. Aluminum was not observed to enter the 2212 lattice to the limits of detection, and the T_c and superconducting properties of films compared closely to reference films measured without $(Sr,Ca)_3Al_2O_6$ defect addition. Formation of $(Sr,Ca)_3Al_2O_6$ defects occurred significantly only after melting was initiated for most compositions. The $(Sr,Ca)_3Al_2O_6$ defects formed were about 0.2 to 2 μm in size, depending on precursor composition and process temperature. The $(Sr,Ca)_3Al_2O_6$ defects increased in size (coarsened) with higher melt temperature process profiles. The Sr:Ca ratio of $(Sr,Ca)_3Al_2O_6$ was observed to remain constant after formation for a range of melt temperatures (approximately 865 to 890 °C). Addition of $(Sr,Ca)_3Al_2O_6$ defects provided a means to reduce secondary Bi–Sr–Ca–Cu–O defect volume fractions by factors of 2 to 6 and significantly improved flux pinning properties at 20–30 K temperature and 0–2 T applied field. The improvement for 25% volume fraction addition of $(Sr,Ca)_3Al_2O_6$ to $Bi_2Sr_2CaCu_2O_{8+\delta}$ is within a factor of 0.5 of that achieved for (Bi,Pb)2212 single crystals; however, it is still about one order of magnitude lower than that achieved for irradiated tapes. It is possible that further improvements in flux pinning could be achieved with $(Sr,Ca)_3Al_2O_6$ defects if methods could be developed to reduce $(Sr,Ca)_3Al_2O_6$ defect coarsening.

ACKNOWLEDGMENTS

The authors thank H.J. Brown and R. Drew for assistance with SQUID measurements and Dr. T. Vanderah and Dr. J. Cline for help with x-ray diffraction data collection. Commercial equipment is identified to adequately specify the experimental procedure; recommendation or endorsement by the National Institute of Standards and Technology is not therein implied.

REFERENCES

1. M.S. Walker, D.W. Hazelton, M.T. Gardner, J.A. Rice, D.G. Walker, C.M. Trautwein, N.J. Ternullo, X. Shi, J.M. Weloth, R.S. Sokolowski, and F.A. List, IEEE Trans. Appl. Supercond. **7,** 889 (1997).
2. D.T. Shaw, S. Jin, and M. Murakami, in *Processing and Properties of High T_c Superconductors Volume 1. Bulk Materials*, edited by S. Jin (World Scientific, River Edge, NJ, 1993), pp. 87–120, 213–272.
3. R.L. Meng, C. Garcia, Y.Q. Wang, W.N. Kang, I. Rusakova, and C.W. Chu, Physica C **306,** 223 (1998).
4. K. Heine, J. Tenbrink, and M. Thöner, Appl. Phys. Lett. **55,** 2441 (1989).
5. J. Kase, K. Togano, H. Kumakura, D.R. Dietderich, N. Irisawa, T. Morimoto, and H. Maeda, Jpn. J. Appl. Phys. **29,** L1096 (1990).
6. T. Haugan, *Partial-Melt Growth of $Bi_2Sr_2CaCu_2O_{8+x}$/Ag Superconducting Tapes*, Ph.D. Dissertation, State Univ. of New York at Buffalo (UMI Dissertation Services, Ann Arbor, MI, 1995).
7. T. Haugan, S. Patel, J. Pitsakis, F. Wong, S.J. Chen, and D.T. Shaw, J. Electron. Mater. **24,** 1811 (1995).
8. J. Shimoyama, N. Tomita, T. Morimoto, H. Kitaguchi, H. Kumakura, K. Togano, H. Maeda, K. Nomura, and M. Seido, Jpn. J. Appl. Phys. **31,** L1328 (1992).
9. S. Patel, T. Haugan, S. Chen, F. Wong, E. Narumi, and D.T. Shaw, Cryogenics **34,** 537 (1994).
10. H. Kumakura, K. Togano, H. Kitaguchi, H. Maeda, and J. Kase, Physica C **185–189,** 2341 (1991).
11. L. Krusin-Elbaum, J.R. Thompson, R. Wheeler, A.D. Marwick, C. Li, S. Patel, D.T. Shaw, P. Lisowski, and J. Ullman, Appl. Phys. Lett. **64,** 3331 (1994).
12. W. Wei, J. Schwartz, K.C. Goretta, U. Balachandran, A. Bhargava, Physica C **298,** 279 (1998).
13. T. Haugan, W. Wong-Ng, L.P. Cook, H.J. Brown, L. Swartzendruber, and D.T. Shaw, Physica C **335,** 129 (2000).
14. T. Haugan, W. Wong-Ng, L.P. Cook, L. Swartzendruber, H.J. Brown, and D.T. Shaw, in *Perovskite Oxides for Electronic Energy Conversion, and Energy Efficiency Applications*, edited by W. Wong-Ng, T. Holesinger, G. Riley, and R. Guo (American Ceramic Society Ceramic Transactions **104,** Westerville, OH, 2000).
15. T.G. Holesinger, J. Mater. Res. **11,** 2135 (1996).
16. T. Haugan, W. Wong-Ng, L.P. Cook, R.G. Geyer, H.J. Brown, L. Swartzendruber, and J. Kaduk, IEEE Trans. Appl. Supercond. **11,** 3305 (2001).
17. P.E. Kazin, V.V. Poltavets, Y.D. Tretyakov, M. Jansen, B. Freitag, and W. Mader, Supercond. Sci. Technol. **12,** 475 (1999).
18. K.C. Goretta, M.M. Cuber, L.R. Feng, B.L. Fisher, M. Jiang, M.T. Lanagan, U. Balachandran, Y. Xu, and M. Xu, IEEE Trans. Appl. Supercond. **9,** 1896 (1999).
19. P.E. Kazin, V.V. Poltavets, Y.D. Tretyakov, M. Jansen, B. Freitag, and W. Mader, Physica C **280,** 253 (1997).
20. J.J. Lin, W.Y. Lin, and R.F. Tsui, Physica C **210,** 455 (1993).
21. S.X. Dou, H.K. Liu, S.J. Guo, K.E. Easterling, and J. Mikael, Supercond. Sci. Technol. **2,** 274 (1989).
22. Y. He, F. Zhou, and Z.X. Zhao, Physica C **328,** 207 (1999).
23. S. Lee, K.J. Kwon, W.S. Kim, and S.I. Lee, Physica C **251,** 149 (1995).
24. I. Matsubara, R. Funahashi, T. Ogura, H. Yamashita, K. Tsuru, and T. Kawai, J. Cryst. Growth **141,** 131 (1994).
25. Y. Abe, K. Hirata, H. Hosono, and Y. Kubo, J. Mater. Res. **7,** 1599 (1992).
26. J.A. Alarco, A. Ilushechkin. T. Yamashita, A. Bhargava, J. Barry, and I.D.R. MacKinnon, J. Mater. Sci. **32,** 3759 (1997).
27. R.D. Shannon, Acta Crystallogr. A **32,** 751 (1976).
28. Powder Diffraction File Nos. 24-1187 and 28-1429 (International Centre for Diffraction Data, Newtown Square, PA).
29. K.F.J. Heinrich, *Electron Beam X-ray Microanalysis* (Van Nostrand Reinhold, New York, 1981).
30. T. Morimoto, J. Shimoyama, J. Kase, and E. Yanagisawa, Supercond. Sci. Technol. **5,** S328 (1992).
31. P. Majewski, Adv. Mater. **6,** 460 (1994).
32. T.G. Holesinger, D.J. Miller, and L.S. Chumbley, Physica C **217,** 85 (1993).
33. R. Müller, Th. Schweizer, P. Bohac, R.O. Suzuki, and L.J. Gauckler, Physica C **203,** 299 (1992).
34. D.C. Sinclair, J.T.S. Irvine, and A.R. West, J. Mater. Chem. **2,** 579 (1992).
35. K. Knížek. E. Pollert, D. Sedmidubský, J. Hejtmánek, and J. Prachaová, Physica C **216,** 211 (1993).
36. *Certificate of Analysis*, *S.R.M. 660*, edited by C.R. Hubbard, Y. Zhang, and R.L. McKenzie (National Institute of Standards and Technology, Gaithersburg, MD, 1989), p. 20899.
37. M.D. Vaudin, M.W. Rupich, M. Jowett, G.N. Riley, and J.F. Bingert, J. Mater. Res. **13,** 2910 (1998).
38. M.D. Vaudin, Proc. Int. Conf. Textures Mater, 12th **1,** 186 (1999).
39. TexturePlus: available on http://www.ceramics.nist.gov/webbook/TexturePlus/texture.htm.
40. M.D. Vaudin and G.R. Fox, in *Ferroelectric Thin Films VIII*, edited by R.W. Schwarz, P.C. McIntyre, Y. Miyasaka, S.R. Summerfelt, and D. Wouters (Mater. Res. Soc. Proc. **596,** Warrendale, PA, 2000), pp. 363–368.
41. T. Fahr, W. Pitschke, H.-P. Trinks, and K. Fischer (Inst. Of Phys. Publishing Conf. Ser. **167,** Philadelphia, PA, 2000), p. 587.
42. M. Onoda, A.Yamamoto, E. Takayama-Muromachi, and S. Takekawa, Jpn. J. Appl. Phys. **27,** L833 (1988).
43. D.P. Matheis and R.L. Snyder, Powder Diffr. **5,** 8 (1990).
44. C.E. Fiori, C.R. Swyt, and R.L. Myklebust, *NIST/NIH Desktop Spectrum Analyzer Program and X-ray Database* (National Institute of Standards and Technology Standard Reference Database **36,** Gaithersburg, MD, 1991).
45. M. Muralidhar, M.R. Koblischka, and M. Murakami, Physica C **313,** 232 (1999).
46. R.B. Goldfarb, M. Lelental, and C.A. Thompson, in *Magnetic Susceptibility of Superconductors and Other Spin Systems* (Plenum, New York, 1991), p. 49.
47. G.S. Grader, E.M. Gyorgy, P.K. Gallagher, H.M. O'Bryan, D.W. Johnson, Jr., S. Sunshine, S.M. Zahurak, S. Jin, and R.C. Sherwood, Phys. Rev. B **38,** 757 (1988).
48. L. Walz, Z. Kristall. **213,** 47 (1998).
49. B.D. Cullity, *Elements of X-Ray Diffraction* (Addison-Wesley, Menlo Park, CA, 1978).
50. W. Zhang, A. Pashitski, and E. Hellstrom, in *Superconductivity and Its Applications*, edited by H.S. Kwok, D.T. Shaw, and M.J. Naughton (American Institute of Physics Conf. Proc. **273,** New York, 1993), p. 599.
51. I. Chong, Z. Hiroi, M. Izumi, J. Shimoyama, Y. Nakayama, K. Kishio, T. Terashima, Y. Bando, and M. Takano, Science **276,** 770 (1997).
52. J. Shimoyama, Y. Nakayam, K. Kitazawa, K. Kishio, Z. Hiroi, I. Chong, and M. Takano, Physica C **281,** 69 (1997).
53. C. Li, S. Patel, J. Ye, E. Narumi, D.T. Shaw, and T. Sato, Appl. Phys. Lett. **63,** 2558 (1993).